12,11,09

Increasing the intensity of the glow of the phosphor $Gd_2O_2S:Tb(3-7\,mol.\%)$, caused by a change in the distribution of the Tb^{3+} activator over the real crystal lattice

© V.V. Bakovets, V.V. Sokolov, I.P. Dolgovesova, T.D. Pivovarova, I.J. Filatova, M.I. Rakhmanova, I.V. Jushina, I.P. Asanov, A.V. Sotnikov

Nikolaev Institute of Inorganic Chemistry, Siberian Branch, Russian Academy of Sciences, Novosibirsk, Russia

E-mail: becambe@niic.nsc.ru

Received May 31, 2022
Revised May 31, 2022
Accepted June 12, 2022

Luminophores $Gd_2O_2S:Tb(3-7\,mol.\%)$, obtained through the stage of sol-gel formation of $Gd_2O_3:Tb$ precursors with their subsequent sulfidation in sulfur vapor with LiF flux at 700°C, showed high luminescence efficiency. The characterization of the obtained samples by a set of physicochemical methods established that an increase in the concentration of the Tb^{3+} activator leads to its specific distribution: over gadolinium vacancies $(V_{Gd})'''$, by replacing Gd^{3+} ions and concentrating it at the boundaries of crystallites. It is noted that in this case, the morphology of crystallites changes, the short-range order of the structural unit of the lattice (Gd_2O_2) changes with the introduction of S^{2-} ions into oxygen vacancies $[V_O]^{\bullet\bullet}$ or the substitution of O^{2-} anions, as a result of which the long-range order of the anionic sublattice is violated and the band gap decreases. At high concentrations of the photoluminescence activator Tb3+ 7 mol.%, radiation quenching does not occur due to the presence of the GdOF and TbOF phases. Variations of these effects with an increase in the Tb^{3+} concentration lead to an increase in the intensity of the emission in the green region of the $^5D_4 \rightarrow {}^7F_j$ transitions and a decrease in the intensity of the emission in the blue region of the $^5D_3 \rightarrow {}^7F_j$ transitions.

Keywords: phosphor $Gd_2O_2S:Tb(3-7\,mol.\%)$, real lattice structure, photoluminescence activator distribution, far infrared spectroscopy, Raman spectroscopy, XPS spectroscopy.

DOI: 10.21883/PSS.2022.11.54210.393

1. Introduction

There are several known methods for the making of phosphors based on oxosulfides of rare earth elements (REE). Some of these methods are used to make REE oxosulfides at relatively low temperatures (up to 290°C) by the decomposition of a complex compound of REE with sulfur-containing ligand [1] or by the deposition of the sulfide product using thiourea of inorganic salts or complex compounds of REE in aqueous or organic solutions [2]. However, these methods have low performance and therefore cannot be used for large-scale production of phosphors for a wide application sphere. More acceptable methods are the methods for the deposition of REE hydroxohydroxides from aqueous solutions of inorganic salts using alkalis, followed by dehydration and dehydroxylation to REE oxides and sulfidation of the obtained precursor at the final synthesis stage using reactant gases CS_2, H_2S or sulfur-containing decomposition products, e.g., ammonium rhodanide [3]. The latter method eliminates the fire hazard and toxicity of production in factory conditions. However, sulfidation rate in this method is very low due to too high temperatures required for the reaction 1350°C. Temperature is reduced by the use of fusing agents Na_2CO_3, Li_2CO_3, Na_3PO_4 in solid-state reactions [4–6,], including LiF with the concentration of 0.01–0.06 wt.% [7]. In the present paper we have used an integrated method for the deposition of Gd hydroxohydroxide, followed by annealing in air to the Gd_2O_3 oxide and its sulfidation with sulfur vapors in a dispersed mixture with LiF. An increased number of different chemical elements in reaction processes complicates the phase composition of the end product, affects the distribution of these elements across the real crystal lattice of the product and must manifest itself in a change of photoluminescent (PL) properties of the phosphor. That's why the goal of the present paper is to analyze morphological, phase and structural changes of the phosphor based on the Gd_2O_2S matrix with Tb^{3+} and F^- impurity ions and to study their influence on PL-properties of the product.

2. Experimental part

Gd dioxosulfide doped with Tb^{3+} was synthesized in two stages. The sol-gel method was used to obtain an oxide precursor. The reagents used in the work were nitrates $Gd(NO_3)_3 \cdot 6H_2O$, $Tb(NO_3)_3 \cdot 5H_2O$ having a content of the main components not less than 99.9% (they were obtained from the corresponding oxides). Synthesis was performed from aqueous solutions of mixtures of

the said salts having the required compositions for the formation of sol-gel solid solutions of hydroxocarbonates $Gd_{1-x}Tb_x(OH)_y(CO_3)_z \cdot n(H_2O)$. To do so, we used a mixture of 0.2 M nitrate solutions, which corresponded to the compositions of the required oxides $Gd_2O_3 : 2xTb^{3+}$ at $x = 3, 5$ and 7 mol.% in relation to the Gd content. A twofold excess of NaOH solution of „extra pure" grade in double-distilled water was used as a precipitator. The obtained product was washed with double-distilled water to a neutral pH. Then the product was dried at 50°C to a constant weight and annealed at 700°C in air. Sulfidation was performed at 960°C 2 h in the following mixture: $Gd_2O_3:Tb + LiF$ (1 wt.%) + sulfur excess (extra pure) till complete sulfur evaporation. The obtained product was washed in hot double-distilled water.

The phase composition of the obtained products was determined by the powder diffractometry method using a XRD-7000 diffractometer (CuK_α-radiation 1.5406 Å, Ni-filter, range $5-70°2\theta$, increment 0.03°, accumulation 2 c) made by Shimadzu. Crystallite size was determined according to the revealed coherent scattering region (CSR) using the Hall–Williamson formula. Spectra of far IR-spectroscopy (FIR) were recorded using a VERTEX 80v spectrometer with the spectral resolution of 0.2 cm^{-1}. Powder samples were ground with PE-spectral polyethylene and tablets were pressed. FIR spectra were recorded in pure dry nitrogen atmosphere. The Raman scattering spectra (RS) were obtained using a Spex Triplemate RS-spectrometer (Ar laser, 514 nm). Luminescence spectra (PL) were studied using a Cary Eclipse fluorescence spectrophotometer (made by VARIAN) at room temperature, excitation wavelength $\lambda_{ex} - 290$ nm. Diffuse reflection spectra (DR) $R_d = f(\lambda)$ of powders were recorded by the standard method using a UV-3101PC spectrophotometer (made by Shimadzu) in the range of wavelengths λ from 240 to 800 nm. The accuracy of wavelength axis calibration was ± 0.3 nm for the UV and visible ranges, the reproducibility of wavelength values was ± 0.1 nm. Measurement errors due to light scattering were 0.01%. $BaSO_4$ was used as a reference material. The obtained spectra were corrected to eliminate the edge luminescence using the previously described procedure [8]. The powder DR spectra were used to calculate the samples' optical absorption in relative units using the classical Kubelka–Munk function (K-M) [9] and the band gap (BG) was found using a Tauc plot [10]:

$$\big(F(R_d)\big)\times h\nu\big) = \big(\big((1-R_d)^2/(2R_d)\big) \times h\nu\big) = C(h\nu - \Delta E_g)^n, \quad (1)$$

where R_d is the value of sample's optical reflection in relation to the reference reflection, h is the Planck constant, ν is reflected light wave frequency C is a constant, n is an index of power.

The powders' atomic composition and morphology were studied by energy-dispersion analysis (EDX) using a Hitachi TM3000 TableTop SEM unit with a Bruker QUANTAX 70 EDS add-on device. The chemical composition of the samples' surface and near-surface region was studied using a FLEXPS X-ray photoelectronic spectrometer (Specs, Germany). The spectrometer is equipped with a Phoibos 150 hemispherical electron analyzer and an electron detector with a multichannel plate for 150 channels and a delay line 1-DLD. Spectra were excited by monochromated AlK_α radiation from an X-ray tube with a double anode XR-50M. The transmission energy of the electron analyzer was 20 eV. Measurements were performed at room temperature, system vacuum during shooting of the samples was $\sim 10^{-9}$ mbar. Electron binding energy was measured in relation to an external standard — the line of C 1s = 284.8 eV from the hydrocarbon superficial layer of contaminations, in compliance with the published data [11]. Relative atomic concentrations of elements were calculated using peaks C 1s, O 1s, Gd 4d, S 2s taking into account the electron photoionization cross-section, electron free path length and electron transmission function. For a detailed analysis, the spectra were broken down into symmetrical components which modelled a convolution of the Lorentzian and Gaussian lines. The contribution of spectrum S 2p to Gd 4d was modelled taking into account the line shape for Gd_2O_3. The background of inelastic electron scattering was deduced by the Shirley method.

3. Experimental results

Fig. 1 shows the diffraction patterns of Gd_2O_2S samples doped with PL activator Tb^{3+} having the following concentrations in relation to Gd^{3+} content: 3, 5, 7 mol.%. Then these samples will be marked as GOS:Tb3, GOS:Tb5 GOS:Tb7, whose matrix crystal structure is represented by hexagonal dioxosulfide Gd_2O_2S (PDF 000-26-1422) space group $P\bar{3}m1$ (164) with the lattice unit cell parameters (UC) $a = b = 3.852$ Å; $c = 6.667$ Å), and lattice UC pa-

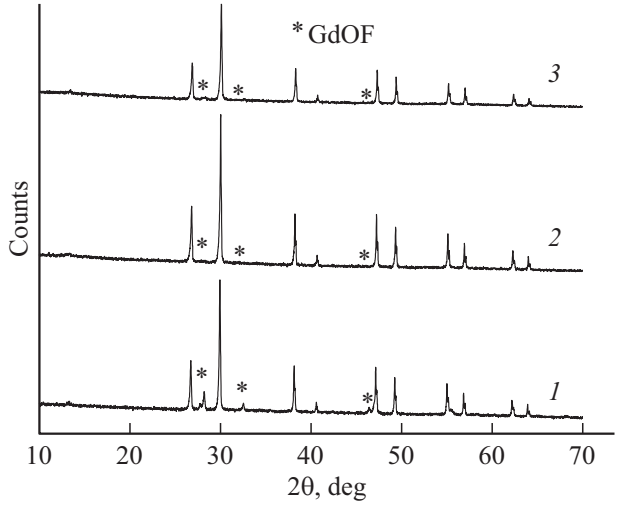

Figure 1. Diffraction patterns for the GOS:Tb3 (*1*), GOS:Tb5 (*2*) and GOS:Tb7 (*3*) samples.

Table 1. UC volume, atomic composition, ratio of the main RS modes and samples' CSR values

Sample	V_{UC}, Å^3	EDX, at.%					RS		CSR, nm
		Gd	O	S	Tb	F	R_1/R_3, ±0.02	R_2/R_4, ±0.02	
GOS:Tb3*	99.351	46.9	27.4	20.9	3.1	1.4	1.91	1.69	273
GOS:Tb5	98.586	48.9	23.6	22.0	5.2	< 1	1.97	1.75	398
GOS:Tb7	98.652	47.6	24.3	21.1	5.8	1.2	1.97	1.65	290
		XPES, at.%					–		
GOS:Tb3		40.1	45.7	14.3	5.6	**	–	–	

Note. * For the reference sample of Gd_2O_2S $V_{UC} = a^2c = 98.924$ Å^3 (PDF 26-1422). ** Concentration is low for a quantitative estimation.

rameters of the GOS:Tb3, GOS:Tb5 and GOS:Tb7 samples: $a = 3.858(2)$ Å, $c = 6.675(3)$ Å; $a = 3.848(2)$ AA, $c = 6.658(3)$ Å and $a = 3.849(2)$ Å, $c = 6.659(3)$ Å, respectively. The values of unit cell volumes V_{UC} are given in Table 1. The diffraction pattern processing computer software shows the presence of an impurity phase with reflections at the angles of $2\theta = 27.7$, 28.2, 32.6 and 46.4 deg. The impurity phase reflections are not seen in the figures, except the GOS:Tb3 sample, since its concentration is low and is at the diffractometer resolution level of 1 wt.%. The impurity phase is not eliminated by repeated product washing and additional annealing for 6 h at 1200°C in sulfur vapors. The position of the impurity phase reflections corresponds to the GdOF phase (space group $R\bar{3}m$ (166) ICSD 184007), which forms in a concurrent reaction of Gd_2O_3 with LiF fusing agent in the course of oxide sulfidation, similarly to interaction with NH_4F [12], as distinct from the conjecture of inclusion of F^- ions into the Gd_2O_2S matrix lattice [7]. It can be assumed that the TbOF impurity phase forms also at increased concentrations of Tb^{3+} ions. Of course, the used methods for the characterization of reaction products do not allow for separating these impurity phases due to their identical structural and physical properties. An increase of terbium content from 3 to 5 and 7 mol.% in the system causes an increase of the lattice UC parameter a and a decrease of the parameter c. Values of these parameters exceed the parameters a and c of the reference Gd_2O_2S. Along with that, there is a change of the reflections' width at half maximum, which is due to a change of CSR and, consequently, a change of crystallite sizes. Indeed, the average CSR value for the GOS:Tb3, GOS:Tb5 and GOS:Tb7 samples is in the region of 273–398 nm (Table 1). The given estimated CSR values are not identical to the true crystallite sizes due to the fact that the reflection widening values are comparable to these parameters for the Si-reference. However, the relative change of the given values is proportional to the change of crystallite sizes in different samples. Moreover, a solid solution forms, since the trigonal phase Tb_2O_2S (space group $P\bar{3}m1$ (164) ICSD 109331) has the UC parameters $a = 3.8249(5)$ Å and $c = 6.6260(8)$ Å which are close to the matrix UC parameters, while the angles 2θ are slightly greater. The study of the morphology of the powders (Fig. 2) and CSR has shown that the particles are mainly represented by crystallite aggregates.

When the concentration of Tb^{3+} ions in the system increases from 3 to 5 and 7 mol.%, the particle distribution maximum shifts towards smaller sizes from 2.00 to 1.30, but then increases to 1.38 μm.

Table 1 gives the EDX data which shows that the amount of F impurity in the GOS:Tb3 and GOS:Tb7 samples is 1.47 and 1.15 at.%, while this level in the GOS:5 sample is below the error of chemical composition determination by the EDX method $\sim$ 1 at.%.

The EDX results have revealed an inexplicable effect of a small oxygen content in the samples (see Table 1) — it is 2 times smaller than the reference Gd_2O_2S. Our EDX spectrum is similar to the one obtained in [13], however, the authors paid no attention to the decreased oxygen content. The mismatch of the XRD results with the EDX results is probably related to an overlap of the O^{2-} peak onto the peak of another ion within the capabilities of the spectrum machine processing software. Due to this, we have analyzed the composition of the obtained product GdOS:Tb3 by the XPES method, and the analysis results (Fig. 3) have confirmed the oxygen composition close to the anticipated one for the given compound (Table 1). However, an increased sulfur content is observed. This effect is probably related to the fact that the region of the 169 eV energies has a wide peak of non-elastic losses of the Gd 4d spectrum, which partially overlaps the spectrum of sulfur S 2p (Fig. 3, A), and there is an overlap of the sulfate sulfur peak (Fig. 2, b). A quantitative analysis of the composition of the main compound was performed without consideration of the molecular forms located on the sample surface: SO_4^{2-}, carbonate anions and hydrocarbons. Carbon is a process-related impurity caused by sample sintering in a glass-carbon container.

Fig. 4 shows the PL spectra of the GOS:Tb3, GOS:5, GOS:7 samples and the reference industrial sample Gd_2O_2S:Tb3% (Toshiba G brand). All the spectra were normalized in terms of intensity.

The excitation band $\lambda_{ex} = 290$ nm was chosen on the main emission band $\lambda_{em} = 542$ nm in compliance with the excitation spectra. The PL 542 nm band has the highest intensity and corresponds to transitions of the $4f-5d$

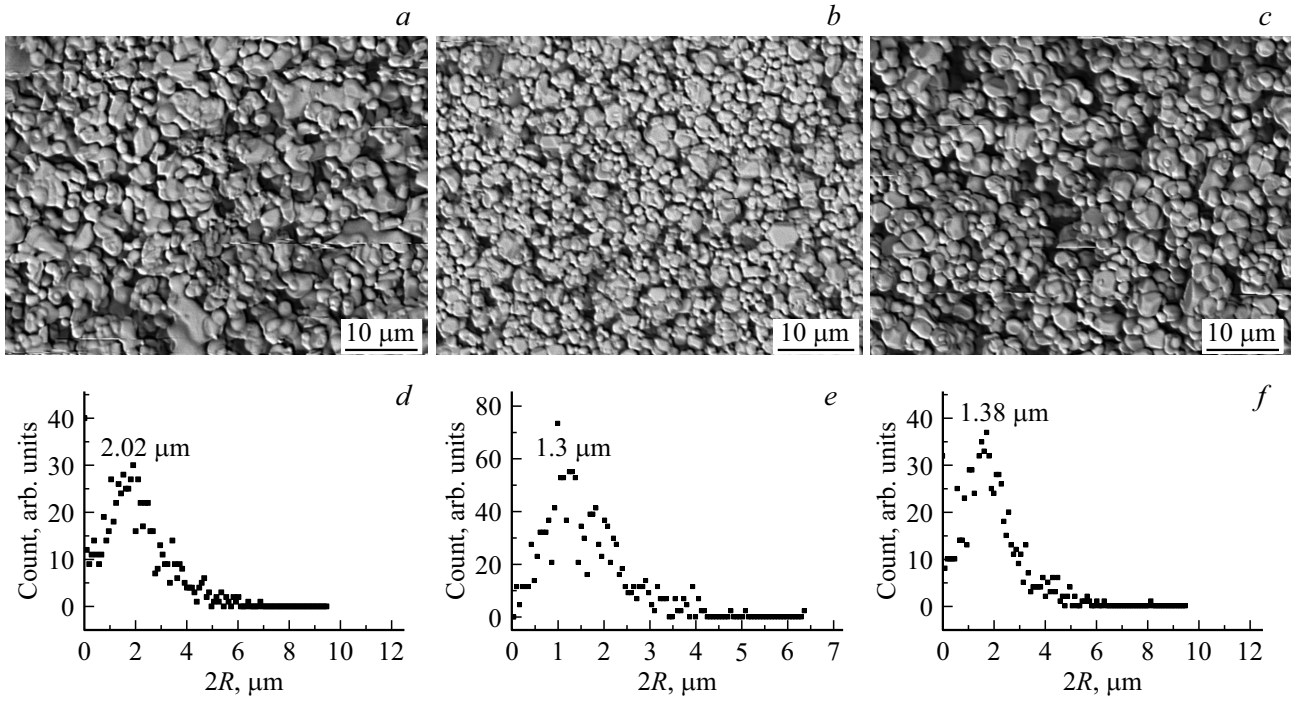

Figure 2. Powder morphology according to SEM (*a, b, c*) and particle size distribution (*d, e, f*). GOS:Tb3 (*a, d*), GOS:Tb5 (*b, e*) and GOS:Tb7 samples (*c, f*).

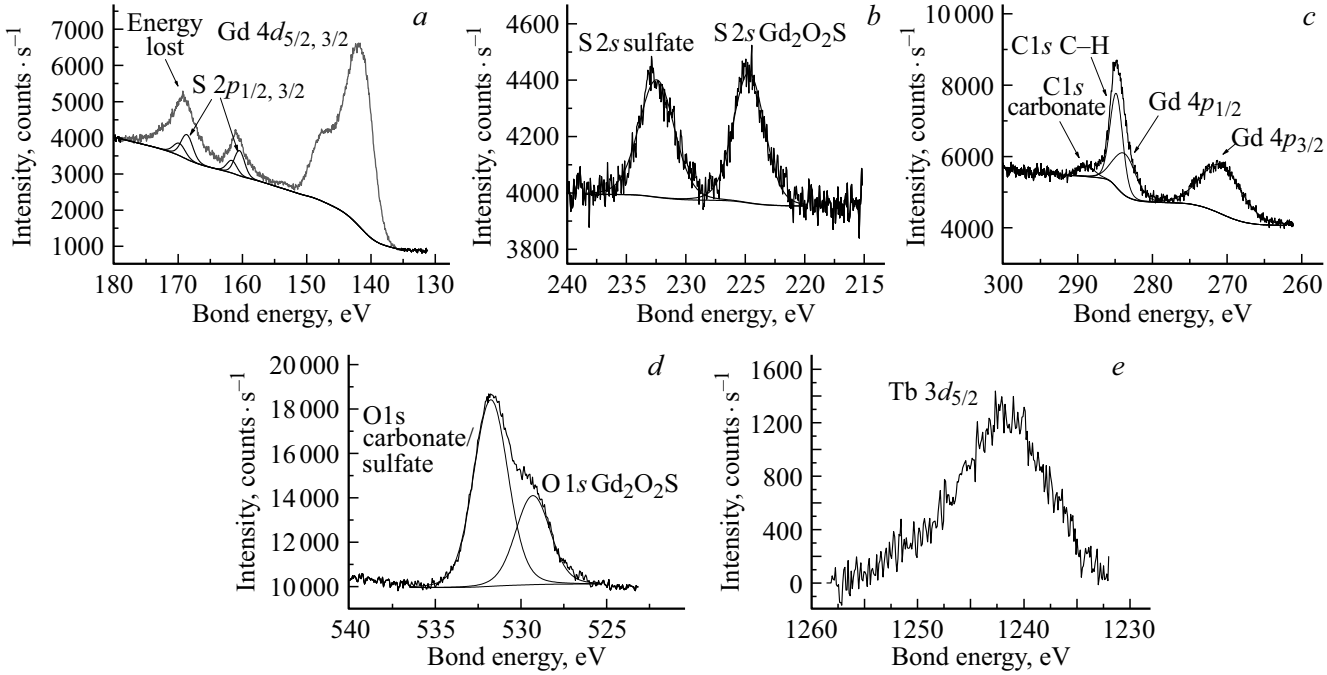

Figure 3. XPES spectra of the GOS:Tb3 sample.

level charges of Tb^{3+} ions [14–17] with excitation energy transfer to their ^5D_j-levels. Thereat, the increase of PL band intensity in the green spectrum region > 490 nm is confirmed at Tb^{3+} ion concentrations of > 3 mol.% [18] due to an increase in the population of $^5D_4 - {}^7F_j$ transitions in relation to $^5D_3 - {}^7F_j$ transitions [17]. This effect was found previously [19] for the $Y_2O_2S:Tb$ compound, but was not checked for the Gd_2O_2S compound. It was concluded that energy transfer to the optically active level $^5D_3$ is not affected by the nearby level $^5D_4$, at least, up to the Tb^{3+} concentrations $> 0.25\%$. This influence in the form of exchange interactions with the dissipation of excitation

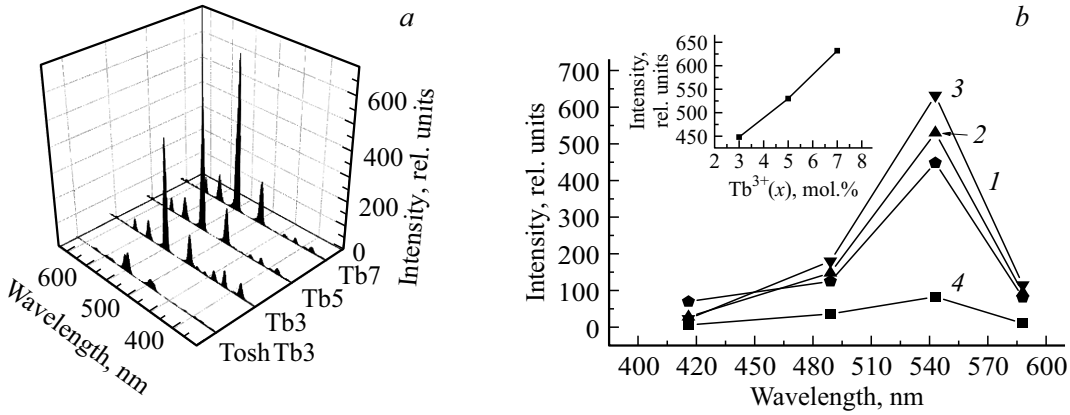

Figure 4. PL spectra of the samples at $\lambda_{ex} = 290$ nm (a), change in intensity of the main PL bands with a change of Tb^{3+} concentration: 3 (*1*), 5 (*2*), 7 mol.% (*3*) (b). The inset shows the PL intensity for the 542 nm band vs. concentration of Tb^{3+}.

energy of the level $^5D_3$ of Tb^{3+} ions manifests itself at their high concentration, so that the excitation energy of $^5D_3 \rightarrow {}^7F_j$ radiative transitions is insufficient. At the same time, PL quenching in the region of > 490 nm is not observed in our case when the Tb^{3+} concentration is above 3 mol.%, while the intensity of the main PL band of 542 nm increases linearly (Fig. 4, b). Thus, when the concentration of Tb^{3+} ions in the system increases, the known maximum limit of concentration quenching development, previously determined as < 4.5 mol.% [20,19] or 1 mol.% [21], is not present in our case, at the least, up to 7 mol.%, the same as in [22]. It appears that when the GdOF : Tb^{3+} impurity (and/or TbOF) is present, channels of radiative transition excitation transfer in Tb^{3+} ions change with the participation of lanthanoid oxofluoride levels. The GdOF compound is known to be a good matrix for PL activators Tb^{3+} and Eu^{3+} [23]. Thereat, the appearance of the excitation spectra at the PL band of 542 nm is virtually unchanged. Predominant PL excitation occurs due to $4f-4f$ and $4f-5d$ transitions of Tb^{3+} ions in Gd_2O_2S sublattices of the matrix and GdOF : Tb^{3+} impurity. Fig. 4, a and b show that the PL band intensity for the GOS : Tb3 sample is 5 times higher than that for the Toshiba (G) reference sample. When excitation wavelength changes to 280 and 240 nm, the ratio of PL band intensities is virtually unchanged, but the intensities themselves increase in magnitude. Thereat, PL quenching is not observed, while excitation energy is also transferred with the participation of Gd^{3+} ions of the Gd_2O_2S matrix [15].

Since lattice volume V_{UC} (Table 1), X-ray diffraction pattern and PL spectra of the samples change with an increase of the concentration of Tb^{3+} ions, it is interesting to analyze the change of chemical bonds using infrared spectroscopy. Since the Gd–O, Gd–S, Tb–O, Tb–S, Gd–F and Tb–F bonds are well resolved in the far-infrared region(FIR), we studied this region of optical spectroscopy. The authors of [22] point out the fact that Gd-S bonds manifest themselves at wave numbers $< 300\,cm^{-1}$, while Gd–O bonds manifest themselves at $> 300\,cm^{-1}$. According to other data, the weak absorption bands of 260, 430, 460 and $510\,cm^{-1}$ FIR pertain to Gd–O, Gd–F dipole bonds of Gd_2O_2S and GdOF compounds [5,23]. Fig. 5 shows the FIR-spectra of the obtained samples. As is known [22], the short-range order structure of hexagonal oxosulfide Gd_2O_2S resembles the structure of cubic sesquioxide C-Gd_2O_3 with a distorted coordination sphere of the cation due to a partial substitution of O^{2-} ions by S^{2-} ions. It is known [24] that the region of $90-140\,cm^{-1}$ for REE sesquioxides of the cubic modification, and gadolinium in particular, pertains to cation movement, while the region of $200-280\,cm^{-1}$ pertains to anion movement. The region of $400-600\,cm^{-1}$ corresponds to absorption by tetrahedral and octahedral groupings. It appears that the said regions will pertain to oxosulfides [22,5]. In compliance with this, the FIR-spectra can be interpreted as follows. The cation sublattice does not greatly change with an increase of Tb^{3+} concentration, but the intensity of anion sublattice bands increases by an order, which indicates its considerable rearrangement.

In addition to the FIR-spectra, we have analyzed the RS spectra (Fig. 6). A series of bands of 347, 363, 380, 509, 524, 668, 708, 717, 883 and $912\,cm^{-1}$ is observed at the Tb^{3+} concentration of 3 mol.%. These bands have a very low intensity for the GOS : Tb5 and GOS : Tb7 samples where the concentration of the GdOF impurity phase is considerably lower. That's why these bands can be ascribed to the GdOF impurity phase. In compliance with the presented description of the RS spectra of Gd_2O_2S and Gd_2O_2S : Eu(0.1, 5.0%) [25], the main groups with unchanged centers of mass in the symmetry operation D_{3d} are S atoms and the Gd_2O_2 parallelogram. The Raman-active modes in this structure are the internal modes of a parallelogram: $R_1 = E_g(Q_2, Q_3)$, $R_2 = A_{1g}(Q_1)$, $R_3 = E_g(Q_5, Q_6)$ and $R_4 = A_{1g}(Q_4)$, where Q_1, Q_2, Q_4 and Q_5 [25] reflect the atomic motion in the plane of the Gd_2O_2 parallelogram and Q_3, Q_6 — atomic motion in the direction of the normal to this plane. To understand the nature of phonon spectrum changes with an increase of Tb^{3+} concentration, we analyzed the ratios

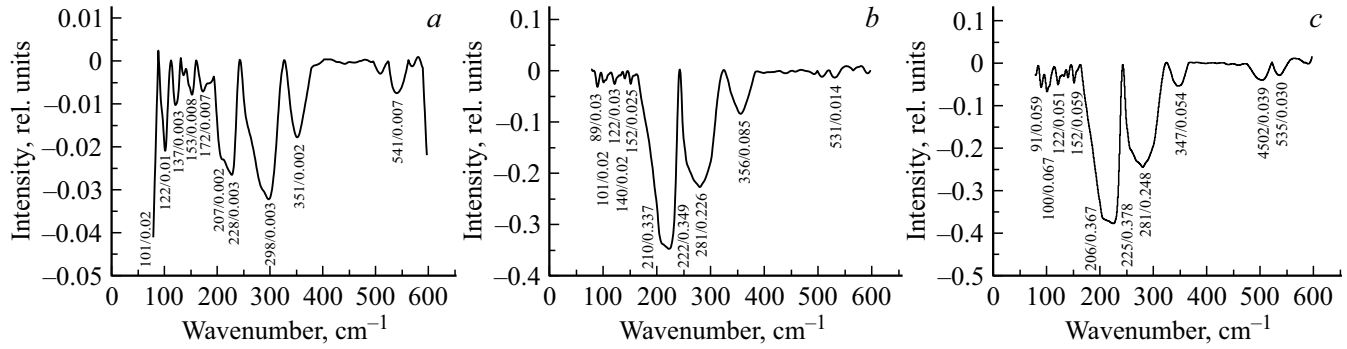

Figure 5. FIR spectra of the samples: GOS:Tb3 (*a*), GOS:Tb5 (*b*) GOS:Tb7 (*c*).

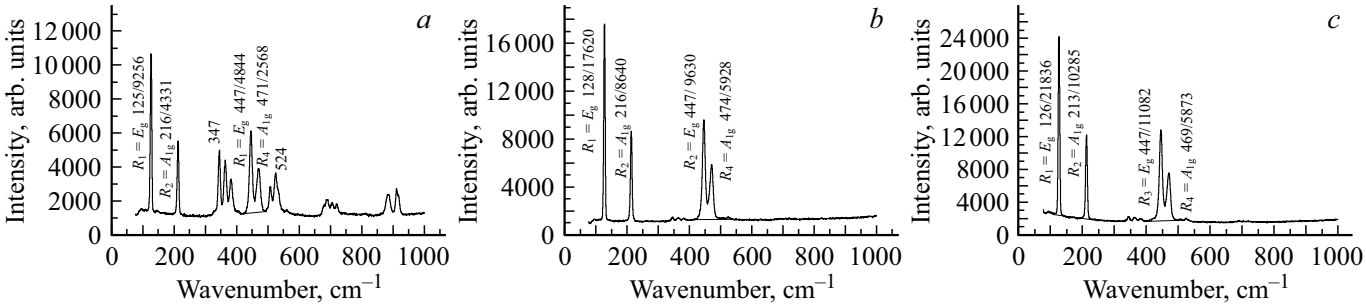

Figure 6. RS spectra of the samples: GOS:Tb3 (*a*), GOS:Tb5 (*b*) and GOS:Tb7 (*c*).

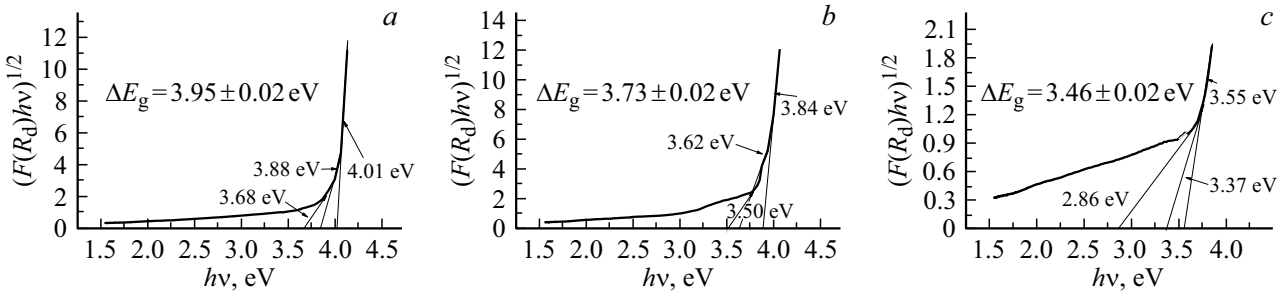

Figure 7. Diffuse reflection spectra of the samples: GOS:Tb3 (*a*), GOS:Tb5 (*b*) and GOS:Tb7 (*c*).

of intensities of normal vibration modes A_{1g} and E_g: R_1/R_3 and R_2/R_4 (see Table 1). It can be seen that the R_1/R_3 ratio increases with a concentration increase from 3 to 5 mol.% and remains constant up to 7 mol.%, which correlates with the change of the ratio of the band intensities in the low-frequency and high-frequency FIR regions. The R_2/R_4 ratio increases under a transition from 3 to 5 mol.% and decreases at 7 mol.%.

Optical band gap ΔE_g is one of the basic characteristics of dielectrics and semiconductors which gives an insight into the nature of charge carrier transfer from the valent state band into the conduction band. Fig. 7 shows the samples' diffuse reflection spectra in $\left(F(R_d) \times h\nu\right)^{1/2} - h\nu$ coordinates. The matrix of the $Gd_2O_2S:Tb$ compound is characterized by indirect charge transitions [26], that's why the band gap is found as the average value between $[(\Delta E_g + \varepsilon_{Ph}) + (\Delta E_g - \varepsilon_{Ph})]/2$, where ε_{Ph} is the energy of phonons involved in charge transfer, $(\Delta E_g + \varepsilon_{Ph})$ and $(\Delta E_g - \varepsilon_{Ph})$ are the values of the points of intersection of the tangents to the straight-line curve portions with the axis of abscissas [27]. Accordingly, the values of ε_{Ph} are determined by a deduction of these components (Table 2).

The obtained results show that the band gap ΔE_g of the $Gd_2O_2S:Tb$ compounds decreases with an increase of Tb^{3+} ion concentration and is small as compared to the pure matrix 4.3–4.6 eV [26,7]. A band-band charge transition takes place with the participation of phonons, and phonon energy increases with an increase of the Tb^{3+} ion concentration from 3 to 5 mol.% and then remains constant up to 7 mol.%. Thereat, an exciton can form at the long-wave fundamental absorption edge with emission of a phonon having the energy $h\nu_{Ph} = \Delta E_g + \varepsilon_{Ph} - E_{ex}$ [27] (Table 2).

Table 2. Band gap ΔE_g, phonon energies ε_{Ph}, exciton energies E_{ex} and energies of emitted phonons $h\nu_{\text{Ph}}$

Sample	$\Delta E_g + \varepsilon_{\text{Ph}}$, eV; $R^{2,*}$	$\Delta E_g - \varepsilon_{\text{Ph}}$, eV, R^2	ΔE_g, ± 0.02, eV	ε_{Ph}, ± 0.02, eV	E_{ex}, R^2	$h\nu_{\text{Ph}}$, eV
GOS:Tb3	4.01; 1.000	3.88; 1.000	3.95	0.07	3.68; 0.997	0.33
GOS:Tb5	3.84; 1.000	3.62; 0.976	3.73	0.11	3.50; 0.953	0.34
GOS:Tb7	3.55; 1.000	3.37; 0.991	3.46	0.11	2.86; 0.986	0.69

Note. $^*R^2$ is the squared regression coefficient for the plotting of tangents to a curve as per tabular data of the chosen segments of function $(F(R_d) \times h\nu)^{1/2} - h\nu$.

4. Discussion of results

Gd_2O_2S:Tb phosphors in our case were synthesized by the mechanism of a topochemical heterogenous reaction — sulfidation of the C-Gd_2O_3:Tb solid solution. Synthesis was performed by the partial substitution of oxygen ions by sulfur ions at an increased temperature. Sulfur delivery and oxygen withdrawal were performed by the diffusion of components along crystallite boundaries and by relay-race substitution of one type of O^{2-} anions by another S^{2-}. The process included a reconstruction of the long-range order while the short-range order of cations was relatively unchanged [22] — the structural lattice unit, a parallelogram (Gd_2O_2), was maintained with insignificant changes of bond lengths. A significant rearrangement of the long-range order in this case takes place across the anionic sublattice (a comparison of the FIR-spectra of Gd_2O_2S:Tb (Fig. 5) and Gd_2O_3:Tb,Eu compounds [24]. It is known that the reconstruction of the long-range order of the C-Gd_2O_3 matrix into a Gd_2O_2S matrix is accompanied with the formation of rather a large number of cationic and anionic vacancies $Ln_{2-x}[\,]_xO_{2-y}[\,]_{2-y}S_{1-z}[\,]_{1-z}S^o_w$ [28,29]. The quantity of cation vacancies reaches 2 mol.%. Anionic vacancies during lattice reconstruction facilitate the relay-race diffusion of anions. Probably, it is energetically more favorable for Tb^{3+} ions to fill cationic vacancies of the matrix at low concentrations. Considering the fact that cation radii are $R(Gd^{3+}) = 1.00\,\text{Å} > R(Tb^{3+}) = 0.98\,\text{Å}$ at the coordination number 7 [30], the observed increase of the UC volume (Table 1) can be explained by filling of vacancies $[V_{\text{Gd}}]'''$ at low concentrations of the PL activator for Tb^{3+} ions equal to 3 mol.%. A description of the mechanism of charge change compensation requires in-depth studies for the given system in elaboration of the results of papers [28,29], but this is outside the scope of the present paper. We can conventionally adopt the variant of filling of $[V_{\text{O}}]^{\bullet\bullet}$ and/or $[V_{\text{S}}]^{\bullet\bullet}$ vacancies with O^{2-} or S^{2-} anions in the required correlation. At the same time, Gd and Tb oxofluorides also form at the crystallite boundaries due to the partial decomposition of a fusing agent LiF, which is shown in the diffraction patterns and RS-spectra. The width of the BG-matrix decreases due to the formation of an impurity band of Tb^{3+} ions in it (Table 2).

When concentrations of Tb^{3+} ions are 5 mol.%, the concentration of vacancies $[V_{\text{Gd}}]'''$ decreases, and substitution of Gd^{3+} ions in the cationic sublattice begins. Thereat, the UC volume decreases, matrix crystallinity increases (CSR increases), the anionic sublattice changes (see the FIR-spectra in Fig. 5), phonon energy ε_{Ph} increases. A decrease of the level of GdOF impurity content is observed (Fig. 1 and Table 1). The BG continues decreasing due to the population of the levels of the Tb^{3+} impurity band, and there is an increase in the ratios of RS intensities of the longitudinal and transverse modes $R_2(A_{1g})/R_4(A_{1g})$ — parallel to the c axis and $R_1(E_g)/R_3(E_g)$ perpendicularly to this axis. The excitonic component of charge transition excitation decreases. The combination of these facts shows the peculiarities of rearrangement of the sample's crystalline and electronic structures. Since the cation substitution energy is higher than the energy of embedding of Tb^{3+} ions into vacancies, the process is slower and the accumulation of Tb^{3+} ions at crystallite boundaries, probably, blocks the diffusion of F^- ions into the crystallite bulk with the formation of a GdOF impurity phase which also acts as an efficient matrix for the PL-activator Tb^{3+}. On the whole, activator concentration increases, and intensity of the 542 nm PL band increases with an increase of sample crystallinity degree, while an increase in phonon energy causes the dissipation of the energy required for efficient excitation of $^5D_3 \rightarrow {}^7F_j$ radiative transitions. Thereat, the intensity of the < 450 nm bands decreases.

A further increase of Tb^{3+} concentration to 7 mol.% is accompanied with a decrease of CSR, decrease of the ratio of phonon mode band intensity $R_2(A_{1g})/R_4(A_{1g})$, which indicates a rearrangement of the short-range order of cations. There is a decrease in the BG value ΔE_g while ε_{Ph} is constant, a decrease of E_{ex} and an increase of $h\nu_{\text{Ph}}$. The decrease of CSR characterizes the decrease of crystallite sizes and, respectively, the increase of the specific surface area of crystallites (Table 1). This is determined by an inhibitory limitation of crystallite growth rate at an increased concentration of Tb^{3+} ions at the crystallite boundaries. An

increase in the concentration of these ions at boundaries can be due to energy difficulties in the substitution of Gd^{3+} ions by Tb^{3+} ions under exchange interactions of the latter with each other at increased concentrations. A similar inhibitory effect of Tb^{3+} has been noted earlier for the Gd_2O_3 matrix [31–33]. Implantation of Tb^{3+} ions into lattice interstices by the Frenkel model is obviously hindered energetically. Along with that, an increase in the UC volume is observed; it can be related to a partial substitution of O^{2-} anions in the parallelogram $[Gd_2O_2]$ by S^{2-} anions or to the implantation of S^0 atoms into interstices according to the Frenkel mechanism [28,29] with a change of the BG electronic structure. Thereat, the symmetry of internal vibrations of the parallelogram (Gd_2OS) must change in relation to the reference one (Gd_2O_2), which is confirmed by a change in the vibrational mode ratio $R_2(A_{1g})/R_4(A_{1g})$ parallel to the c axis of the lattice (Table 1).

A further increase of intensity of the 542 nm PL bands and a decrease of intensity of the < 490 nm bands is probably due to an extension of the impurity band in the BG, which determines a decrease of the energy required to pass through it. The latter means an increase of excitation energy of $4f-4f5d$-transitions of Tb^{3+} ions, which causes an increase of the population and, consequently, an increase of intensity of $^5D_4 \rightarrow {}^7F_j$ radiative transitions, particularly the $^5D_4 \rightarrow {}^7F_5$ transition (the 542 nm band). Withdrawal of the PL quenching limit in this case, according to the above-mentioned facts, is probably facilitated by the GdOF:Tb impurity phase, which is an efficient matrix for Ln^{3+} activators of PL [23,34] or the TbOF phase.

5. Conclusion

An integrated method for phosphor synthesis on the basis of a Gd_2O_2S matrix with the addition of a fusing agent LiF 1 mol.% at the sulfidation stage and an increase of concentration of the PL-activator Tb^{3+} to 7 mol.% allow for increasing the PL intensity in relation to the known Toshiba (G) phosphor. This effect is probably achieved due to the participation of GdOF and TbOF impurity phases in population of the main $^5D_4 \rightarrow {}^7F_5$ radiative transition of Tb^{3+} ions and redistribution of Tb^{3+} ions across the vacancy cation sublattice of the main Gd_2O_2S matrix, their concentration being about 3 mol.%. With an increase of Tb^{3+} concentration to 5 mol.%, the impurity implantation mechanism is mainly related to the substitution of matrix cations. Thereat, the blocking of the flow of F^- ions to the main matrix increases because Tb^{3+} ions are concentrated on the crystallite surface. This results in an increase of the product crystallinity degree. When Tb^{3+} concentration further increases to 7 mol.%, S^{2-} ions start substituting oxygen ions, which leads to a change of the short-range order of the cation sublattice, and phonon energy increases. This reduces the energy of excitation of $^5D_3 \rightarrow {}^7F_j$ radiative transitions. Due to this and with the participation of charge transitions from the levels of Tb^{3+} ions of $GdOF:Tb^{3+}$ and TbOF impurity phases, the population of the $^5D_4 \rightarrow {}^7F_5$ radiative transition (the 542 nm band) increases, which causes an increase of phosphor luminescence intensity.

Acknowledgments

The authors would like to thank B.A. Kolesov for recording of the Raman scattering spectra, I.V. Korolkov for X-ray phase analysis, L.A. Sheludyakova for recording of IR-spectra, A.D. Sidorenko for recording of XPS spectra.

Funding

The work was supported by the Ministry of Science and Higher Education of the Russian Federation № 121031700315-2.

Conflict of interest

The authors declare that they have no conflict of interest.

References

[1] F. Zhao, M. Yuan, W. Zhang, S. Gao, J. Am. Chem. Soc. **128**, 11758 (2006).
[2] J. Nanomater. Volume. Article ID 2560436, 1–6 (2017).
[3] V.V. Bakovets, T.D. Pivovarova, I.P. Dolgovesova, I.V. Korolkov, O.V. Antonova, S.I. Kozhemyachenko. ZhOKh **88**, *5*, 850 (2018) (in Russian).
[4] E.-J. Popovici, L. Muresan, A. Hristea-Simoc, E. Indrea, M. Vasilescu, M. Nazarov, D.Y. Jeon. Opt. Mater. **27**, 559 (2004).
[5] G.V. Ananyeva, E.I. Gorokhova, V.A. Demidenko, V.A. Parfinsky, O.A. Khristich. Opt. zhurn. **72**, 68 (2005) (in Russian).
[6] X.-X. Luo, W.-H. Cao, Y. Tian. Opt. Mater. **30**, 351 (2007).
[7] E.I. Gorokhova, G.V. Ananyeva, V.A. Demidenko, S.V. Eronko, E.A. Oreshchenko, O.A. Khristich, P.A. Rodny. Opt. zhurn. **79**, *1*, 58 (2012) (in Russian).
[8] V.V. Bakovets, I.V. Yushina, O.V. Antonova, T.A. Pomelova. Optika i spektroskopiya **121**, 929 (2016) (in Russian).
[9] P. Kubelka, F. Munk. Z. Techn. Phys. **12**, 593 (1931).
[10] J. Tauc, R. Grigorovici, A. Vancu. Phys. Status Solidi **15**, 627 (1966).
[11] D. Barreca et al. Surf. Sci. Spectra **14**, 60 (2007).
[12] L.Ya. Markovsky, E.Ya. Persina, Yu.A. Omelchenko. ZhNKh **16**, *2*, 330 (1971) (in Russian).
[13] Kh.R. Saraee, M.D. Zaden, M. Mostajaboddavati, A.A. Kharieky. J. Electr. Mater. **45**, 4806 (2016).
[14] J. Holsa, M. Leskela, L. Niinisto. Mater. Res. Bull. **14**, 1403 (1979).
[15] S. Chatterjee, V. Shanker, H. Chander. Mater. Chem. Phys. **80**, 719 (2003).
[16] E.I. Gorokhova, V.A. Demidenko, O.A. Khristich. J. Opt. Technol. **70**, 693 (2003).
[17] A. Abreu da Silva, M.A. Cebim, M.R. Davolos. J. Lumin. **128**, 1165 (2008).
[18] E.I. Gorokhova, G.V. Ananyeva, V.A. Demidenko, S.V. Eronko, E.A. Oreshchenko, O.A. Khristich, P.A. Rodny. Opt. zhurn. **79**, *1*, 56 (2012) (in Russian).

[19] Y. Tian, W.-He Cao, X.-X. Luo, Y. Fu. J. Alloys Comp. **433**, 313 (2007).
[20] L. Hernbndez-Adame, A. Mindez-Blas, J. Ruiz-Garcna, J.R. Vega-Acosta, F.J. Medellin-Rodriguez, G. Palestino. Chem. Eng. J. **258**, 136 (2014).
[21] S.-L. Lin, T.-Y. Liu, C.-L. Lo, B.-S. Wang, Y.-J. Lee, K.-Y. Lin, C.A. Chang. http://dx.doi.org/10.1016/j.jlumin.2016.01.037.
[22] X. Sang, G. Xu, J. Lian, N. Wu, X. Zhang, J. He. Solid State Sci. **80**, 15 (2018).
[23] M.I. Gaiduk, V.F. Zolin, L.S. Gaigerova. Spektry lyuminestsentsii evropiya. Nauka, M. (1974). 195 s.(in Russian).
[24] V.V. Bakovets, I.P. Dolgovesova, T.D. Pivovarova, L.A. Sheludyakova. FTT **63**, 2147 (2021) (in Russian).
[25] S. Yokono, S. Syunij, T. Hoshina. J. Phys. Soc. Jpn. **46**, 1882 (1979).
[26] J. Lian, X. Sun, J.-G. Li, B. Xiao, K. Duan. Mater. Chem. Phys. **122**, 354 (2010).
[27] K.V. Shalimova. Fizika poluprovodnikov. Energoatomizdat, M. (1985). 392 s. (in Russian).
[28] Yu.L. Suponitsky, G.M. Kuzmicheva, A.A. Eliseev. Uspekhi khimii **57**, 367 (1988) (in Russian)
[29] G.P. Borodulenko, A.A. Eliseev, V.A. Efremov, G.M. Kuzmicheva, I.V. Perepelkin, N.M. Ponomarev. ZhNKh **30**, 2208 (1985) (in Russian).
[30] R.D. Shanon. Acta Crystall. A **32**, 751 (1976).
[31] A. Garcia-Murillo, A. de J. Morales Ramirez, F. de J. Carrillo Romo, M. Garcia Hernandez, M.A. Dominguez Crespo. Mater. Lett. **63**, 1631 (2009).
[32] P.R. Singh, K. Gupta, A. Pandey, A. Pandey. World J. Nano Sci. Eng. **2**, 13 (2012).
[33] V.V. Bakovets, I.P. Dolgovesova, T.D. Pivovarova, M.I. Rakhmanova. FTT **62**, 2147 (2020) (in Russian).
[34] V.A. Lobach. Zhurn. prikl. spektroskopii **27**, 552 (1977) (in Russian).